INTERNATIONAL JOURNAL FOR NUMERICAL METHODS IN FLUIDS
Int. J. Numer. Meth. Fluids 2001; **37**: 501–523 (DOI: 10.1002/fld.180)

A three-dimensional vortex particle-in-cell method for vortex motions in the vicinity of a wall

Chung Ho Liu*,[1]

Rotating Fluids and Vortex Dynamics Laboratory, Department of Aeronautical Engineering, Chung Cheng Institute of Technology, Taoyuan, Taiwan, Republic of China

SUMMARY

A new vortex particle-in-cell method for the simulation of three-dimensional unsteady incompressible viscous flow is presented. The projection of the vortex strengths onto the mesh is based on volume interpolation. The convection of vorticity is treated as a Lagrangian move operation but one where the velocity of each particle is interpolated from an Eulerian mesh solution of velocity–Poisson equations. The change in vorticity due to diffusion is also computed on the Eulerian mesh and projected back to the particles. Where diffusive fluxes cause vorticity to enter a cell not already containing any particles new particles are created. The surface vorticity and the cancellation of tangential velocity at the plate are related by the Neumann conditions. The basic framework for implementation of the procedure is also introduced where the solution update comprises a sequence of two fractional steps. The method is applied to a problem where an unsteady boundary layer develops under the impact of a vortex ring and comparison is made with the experimental and numerical literature. Copyright © 2001 John Wiley & Sons, Ltd.

KEY WORDS: incompressible flow; vortex motion; vortex particle-in-cell method; vortex ring

1. INTRODUCTION

For many flows, there are distinct rotational and irrotational regions, such as the wake shed from a body. The vortex particle method (see review articles [1]) allows a 'compact' representation of this type of flow field as computational elements may be concentrated in regions of rapid spatial variation. This method involves the use of point vortices or filaments to represent the vorticity field and use related singular functions to approximate solutions of the Navier–Stokes equations at a relatively small viscosity. From the theorems of Kelvin and Helmholtz, vortex lines move with the fluid and vortex tubes are of constant strength. The identification of vortex lines as flow structures with permanent identities naturally leads to a representation

* Correspondence to: Rotating Fluids and Vortex Dynamics Laboratory, Department of Aeronautical Engineering, Chung Cheng Institute of Technology, Tahsi, Taoyuan 335, Taiwan, Republic of China.
[1] E-mail: chliu@ccit.edu.tw

Received May 1999
Revised September 1999

of the flow as an assembly of vortex lines or filaments. The lines or filaments are obtained by the discretization of the regions of vorticity in the flow so that this assembly of 'discrete vortices' is often embedded in an irrotational flow. The main advantage of the vortex methods is that for flows with compact vorticity containing regions no vortices will be needed in the large irrotational region. Thus, an approximation based on the vortex method reduces the mathematical description to its essential components and focuses computational resources on the limited regions of vorticity in the flow rather than on computing the velocity which exists everywhere.

The vortex method has long been used to model unsteady flow in two dimensions, particularly since the work of Chorin [2], and three-dimensional extensions have been considered since the 1980s by others [3–6]. In the two-dimensional case the vortex filaments are all straight lines normal to the plane of motion and so appear as particles within the plane. The method thus reduces to discretizing vorticity onto a collection of particles and tracking their motion in a Lagrangian co-ordinate system. An approximate velocity field is calculated from the Biot-Savart law. The vorticity field is then evolved in time according to this velocity field. In three dimensions however, the stretching and tilting of vortex lines means that as well as computing the motion of the lines account must also be taken of these effects. The first attempt to simulate a flow by using discrete vortices however was by Rosenhead [7] who studied the evolution of a vortex sheet. His hand calculations shown the start of a clear rollup of the vortex sheet, at later times however the motion of the vortices appeared chaotic. This singularity problem spurred the development of the modern vortex method, beginning with the computation of flow past a cylinder by Chorin [2]. A Lagrangian procedure based on tracking vortex filaments was used by Leonard [8] to model the evolution of a turbulent spot in a laminar boundary layer. The results obtained indicated that the inviscid technique successfully reproduced many of the features of the turbulent spot. There are difficulties with this procedure in modeling viscous diffusion, the observed differences between the computation and the experimental results were attributed to poor handling of viscous effects, and the absence of a procedure for creating vorticity at the wall. More recently, attention has focussed on the point vortex representation for three-dimensional flows. In some ways this is an extension of the two-dimensional techniques and much of the prescriptions developed in two dimensions for regularizing the singular particles carry over.

In applying the point vortex technique, there is a choice between purely particle-based treatments for the convection, diffusion, and stretching, and the particle-in-cell (PIC) technique. The latter procedure offers certain advantages in computational efficiency and in treatment of viscosity and is the basis of the technique reported here. For a set of N particles, evaluating the velocity induced at each particle by all the others using the Biot-Savart law has computational cost of $O(N^2)$. Furthermore, the random walk diffusion treatment converges rather slowly. Efficient parallel implementations [9] reduce the time to compute the velocity field, however with large numbers of particles reducing the total computational work is imperative. No-slip boundaries also pose difficulties for particle methods. The vortex PIC method is computationally efficient and simplifies the boundary condition treatment. In our previous work [10,11], it has, in two dimensions, proved to be well suited to computations of unsteady flows. Recently, work [12] has shown the method can be extended to deal with three-dimensional viscous flows in unbounded domain. In this paper, the method will be

extended to study three-dimensional wall bounded viscous flows and its application to the viscous ring–wall interaction problem. Vortex ring–wall interactions have been considered as useful models in studies of boundary layer instability and turbulence and also occur in a variety of applications. Furthermore, they pose a challenge for a numerical scheme in that the numerical procedure has to track the evolution of concentrated vorticity regions that may be ejected away from the wall. Basically, the flow configuration considered herein is complicated in nature. The results could help to shed some light on complex phenomenon and the flow mechanisms involved and serve as a base for further studies on the turbulent boundary layers.

2. MATHEMATIC FORMULATIONS

Taking the curl of the incompressible Navier–Stokes equations leads to the transport equation for vorticity

$$\frac{\partial \vec{\omega}}{\partial t} + \vec{u} \cdot \nabla \vec{\omega} = \vec{\omega} \cdot \nabla \vec{u} + \nu \nabla^2 \vec{\omega} \tag{1}$$

with the constraint

$$\nabla \cdot \vec{\omega} = 0 \tag{2}$$

where $\vec{\omega} = \nabla \wedge \vec{u}$ is the vorticity and ν is the kinematic viscosity.

As the velocity field zero divergence, it may be represented as the curl of a vector potential, so that a Poisson equation relates the vorticity to the velocity to potential. Then the velocity is given as

$$\vec{u}(\vec{x}, t) = \int \mathrm{K}(\vec{x} - \vec{x}')\vec{\omega}(\vec{x}', t)\, \mathrm{d}\vec{x}' \tag{3}$$

where

$$\mathrm{K}(\vec{x}) = \frac{1}{4\pi|\vec{x}|^3} \begin{bmatrix} 0 & x_3 & -x_2 \\ -x_3 & 0 & x_1 \\ x_2 & -x_1 & 0 \end{bmatrix} \tag{4}$$

is the Biot-Savart kernel in three dimensions.

In the point vortex method a set of vortex particles is introduced, of intensity (of strength) $\vec{k}_p$, where the pth particle, $\vec{k}_p = \vec{\omega}_p \delta V$ and δV is an element volume associated with the particle, Thus

$$\vec{\omega}(\vec{x}, t) = \sum_p \vec{\omega}_p(t)\delta V \delta(\vec{x} - \vec{x}_p(t)) = \sum_p \vec{k}_p(t)\delta(\vec{x} - \vec{x}_p(t)) \tag{5}$$

In the pure particle representation, the integral equation (3) reduces to a sum

$$\vec{u}(\vec{x}_i, t) \sum_{j \neq i} \mathrm{K}_\sigma(\vec{x}_i(t) - \vec{x}_j(t)) k_j(t) \tag{6}$$

where $\mathrm{K}_\sigma(\vec{x}) = \mathrm{K}(\vec{x}) * f_r(\vec{x})$ with $\mathrm{K}(\vec{x})$ given in Equation (4) and where $f_r(\vec{x})$ is a smoothing function, equal to unity outside a radius r. Appropriate choices for $f_r(\vec{x})$ are discussed by Winckelmans and Leonard [6] and Hald [13].

In the vortex PIC method, the strengths of the particles are projected onto the nodes of a mesh. In the present scheme, this nodal vorticity is computed using volume interpolation. The velocities at the mesh points are then obtained by solving

$$\nabla^2 \vec{u} = -\nabla \wedge \vec{\omega} \tag{7}$$

A variety of procedures [14–22] have been developed for the velocity–vorticity form of the equations. Given an initial distribution of vorticity, the evolution of the velocity and vorticity may be computed by solving Equations (1) and (7) subjected to appropriate boundary conditions.

3. NUMERICAL FORMULATIONS

3.1. The particle-in-cell method

The vortex PIC method has been successfully used in two-dimensional steady and unsteady viscous flows for both internal [10] and external [11] bounded domain. The three-dimensional versions of PIC methods have been developed and used for inviscid [23–25] and viscous [12] flows. For three-dimensional flows, the vorticity is a vector. This implies that vorticity may be changed by vortex stretching or diffusion as it moves with the flow and therefore we must track vorticity as well as the particle positions. In the present PIC method, an initial vorticity field is discretized as a set of vortex particles, as in the particle methods. The strength of each particle is projected onto the nodes of a fixed Eulerian mesh, and the contributions summed to find the mesh vorticity. The velocity field is then calculated by solving Equation (7) on the mesh, instead of computing the velocity from the Biot-Savart law applied to the set of vortex particles. Thus the present work, combining the mesh based methods techniques with the particle formulation is a hybrid method. However, in comparison with the pure particle method, the mesh effectively smoothes the vorticity over a blob of approximately the cell dimensions. The projection of the vortex strengths onto the mesh is based on volume interpolation. The convection of vorticity is treated as a Lagrangian move operation but one where the velocity of each particle is interpolated from an Eulerian mesh solution of Equation (7). The change in vorticity due to diffusion is also computed on the Eulerian mesh and projected back to the particles. Where diffusive fluxes cause vorticity to enter a cell not already containing any particles new particles are created.

3.2. Implementation of the PIC method

The basic framework for implementation of the procedure is shown below where the solution update comprises a sequence of two fractional steps.

3.2.1. Calculations on Eulerian frame

3.2.1.1. Velocity calculation. The Poisson equations of the velocity are solved by a restarted version of generalized minimal residual method GMRES(m) [26]. Incomplete LU factorizations [27] are used for preconditioning with scaling by the main diagonal pivots of the preconditioner, and the Eisenstat procedure [28] is used to compute the preconditioned matrix–vector multiplication. This Krylov subspace algorithm is an effective iterative method for solving large sparse non-symmetric problems and has an optimal rate of convergence. The discretization of the Poisson equations leads to a large system of equations of the form

$$\boldsymbol{A}\boldsymbol{x} = \boldsymbol{b} \tag{8}$$

where $\boldsymbol{x}$ is the unknown vector and $\boldsymbol{b}$ is the known vector. To solve this linear system, a variant of the preconditioned GMRES is proposed. In the algorithm the two-norm of the residual at each iteration step is minimized. An orthonormal basis generated by the Arnoldi process and the Hessenberg least-squares problem can be solved by Householder transformations. The GMRES(m) algorithm with ILU preconditioner can be summarized as follows.

Algorithm: GMRES(m)-ILU

(1) Start: choose x_0 and let $b = (I + L)^{-1} b$
(2) Iterate: for $n = 0$ until convergence do

$t = (I + U)^{-1} x_n$
$u = t + (I + L)^{-1}((\mathrm{diag}(A) - 2I)t + x_n)$
$r_n = b - u$
$\beta_n = \|r_n\|$
$v_1 = r_n / \beta_n$
for $j = 1, \ldots, m$ do
  $t = (I + U)^{-1} v_j$
  $u = t + (I + L)^{-1}((\mathrm{diag}(A) - 2I)t + v_j)$
  for $I = 1, \ldots, j$ do
    $h_{i,j} = (u, v_i)$
  end do
  $v_{j+1} = u - \Sigma_{i=1}^{j} h_{i,j} v_i$
  $h_{j+1,j} = \|v_{j+1}\|$
  $v_{j+1} = v_{j+1} / h_{j+1,j}$
end do
solve least-squares problem:
$x_{n+1} = x_n + v_m y$, where y minimizes $\|\beta_n e_1 - \overline{H_m} y\|$, $y \in R^m$
and $e_1 = [1, 0, \ldots, 0]^T$
end do

(3) Form the approximate solution: $x_{n+1} = D^{-1/2}(I + U)^{-1} x_{n+1}$

3.2.1.2. Vorticity calculation. The vorticity transport equation (1) can be re-expressed as

$$\frac{\mathrm{D}\vec{\omega}}{\mathrm{D}t} = \vec{\omega}\cdot\nabla\vec{u} + \nu\nabla^2\vec{\omega} \tag{9}$$

where $\mathrm{D}\vec{w}/\mathrm{D}t$ is the material derivative of the vorticity.

In the present method the vorticity is convected explicitly by the moving particles. Thus the explicit discretization of the convection term which causes the smearing of flow features in a purely grid-based method can be avoided. Two alternate forms of the stretching/tilting in Equation (9) have been considered. One is the transpose scheme [29], the other is the mixed scheme [30]. The mixed scheme was advocated by Rehbach [30] since the symmetry of the matrix yields computational savings. In the paper, we adopted the transpose scheme to solve the vorticity stretching/tilting because it leads to exact conservation of the total vorticity, a property not satisfied by the classical scheme of the mixed scheme.

3.2.1.3. Wall boundary conditions. To solve for the velocity $\vec{u}$ in the computational domain D from $\nabla^2\vec{u} = -\nabla\wedge\vec{\omega}$, values of $\vec{u}$ are required on the boundary ∂D. It is useful to distinguish between the treatments of the normal and tangential velocity components. For the normal velocity components, the boundary conditions may be periodic, Dirichlet, or Neumann, and are obviously zero Dirichlet values for a solid wall. For the tangential velocities, at a solid wall it is natural to use Neumann conditions, since this makes relating the surface vorticity to the no-slip velocity condition quite straightforward. In the following, the discretization of the Poisson equation for a tangential velocity component near a no-slip wall is examined. Specifically consider the equation for u_x, (dropping suffix x where possible)

$$\nabla^2 u = -(\nabla\wedge\vec{\omega})_x = \frac{\partial\omega_z}{\partial y} - \frac{\partial\omega_y}{\partial z} \tag{10}$$

with the wall lying in the x–y plane at $z=0$, corresponding to $k=0$ on the mesh. A uniform mesh is considered for simplicity in the discussion, procedures for a stretched mesh being similar. A collocation point, half a mesh length from the wall, is used in setting the vorticity boundary condition. With second-order finite differencing in the normal (i.e., k-) direction, boundary values only enter the discrete equations for $k=1$, and only in the $\partial^2 u/\partial z^2$ (for u) and $\partial\omega_y/\partial z$ (for $(\nabla\wedge\vec{\omega})_x$) terms on the left- and right-hand sides respectively. Clearly these terms must be compatible, and (for simplicity, omitting the discretization of the other terms), we write

$$\left(\frac{\partial^2 u}{\partial x^2} + \frac{\partial^2 u}{\partial y^2}\right)\bigg|_{k=1} + \frac{\dfrac{(u_{i,j,2}-u_{i,j,1})}{\Delta z} - \dfrac{(u_{i,j,1}-u_{i,j,0})}{\Delta z}}{\Delta z} = \frac{\omega_{y(i,j,2)} - \omega_{y(i,j,0)}}{2\Delta z} + \frac{\partial\omega_z}{\partial y}\bigg|_{k=1}$$
$$= \frac{\omega_{y(i,j,3/2)} - \omega_{y(i,j,1/2)}}{\Delta z} + \frac{\partial\omega_z}{\partial y}\bigg|_{k=1} \tag{11}$$

Since we require $\nabla\wedge\vec{u} = \vec{\omega}$ on ∂D, in the discrete equations

$$-\left.\frac{\partial u_z}{\partial x}\right|_{k=1/2}+\left.\frac{\partial u_x}{\partial z}\right|_{k=1/2}$$

should equal $-\omega_{y(i,j,1/2)}$. However close to the wall, $u_z=0$ to order $(\Delta z)^2$, and neglecting

$$-\left.\frac{\partial u_z}{\partial x}\right|_{k=1/2}$$

the discretization of

$$-\left.\frac{\partial u_x}{\partial z}\right|_{k=1/2}$$

i.e., $(u_{i,j,1}-u_{i,j,0})/\Delta z$ should equal $-\omega_{y(i,j,1/2)}$. Assuming this holds we can thus cancel these terms from each side of the equation. Hence the unknown value of the wall vorticity no longer explicitly appears in the discretized Poisson equation and the Dirichlet boundary condition for velocity is effectively replaced by a Neumann condition. The following points arise:

Firstly, the value for the wall vorticity is recovered from the wall velocity condition and with $u_{(i,j,0)}=0$, we obtain

$$\frac{u_{(i,j,1)}}{\Delta z}=\omega_{y(i,j,1/2)}=\frac{\omega_{y(i,j,1)}+\omega_{y(i,j,0)}}{2} \tag{12}$$

hence the wall vorticity used as boundary condition for diffusion in the transport equation follows (with general $u_{(i,j,0)}$) from the $O(\Delta z/2)$ extrapolation

$$\omega_{y(i,j,0)}=-\omega_{y(i,j,1)}+2(u_{i,j,1}-u_{i,j,0})/\Delta z \tag{13}$$

Secondly, the discrete equations are unchanged whether a homogeneous Neumann boundary condition is used or cancellation of the gradient and vorticity boundary conditions in Equation (7) occurs so in this sense the condition is arbitrary.

Thirdly, for each velocity component, Dirichlet boundary values are applied to at least one boundary (e.g. where the particular velocity component is either normal to the boundary or corresponds to an external freestream velocity) so the solution is fully determined in the problems we consider.

For a no-slip wall, we presented a treatment for the discrete equations using a Neumann condition on the velocity gradient, rather than Dirichlet values for velocity. The objective is to use a non-iterative means of setting the vorticity consistent with the no-slip condition. We argue that for the velocity–vorticity formulation, the natural boundary conditions on the tangential velocity at a wall are gradient conditions, since the velocity of fluid at the surface is related to the velocity in the interior of the domain via the vorticity on the surface.

By way of illustration, consider the Stokes problem for the plate, suddenly accelerated to unit velocity. Let z denote the normal direction, and range from 0 at the plate surface, to H at the top boundary. In this case, Equation (7) reduces to

$$\frac{\partial^2 u}{\partial z^2} = \frac{\partial \omega}{\partial z}$$

Initially there is no vorticity in the flow, and so the right-hand side is zero everywhere in the domain [0, H], except at the boundary. Thus a solution with prescribed boundary conditions $u_{z=0} = 1$, $u_{z=L} = 0$, and with zero right-hand side gives the incorrect solution $u(z) = 1 - z/H$, inconsistent with the initial conditions. The reason is that we have ignored the wall vorticity boundary condition required to set the no-slip velocity, and which alters the right-hand side of Equation (7) at the surface. Including this, and calculating the finite difference solution, the boundary condition $u_{z=0} = 1$ is re-expressed as $\mathrm{d}u/\mathrm{d}z = 1/\mathrm{d}z$, and the right-hand side remains 0 except at the wall, where it becomes $1/\mathrm{d}z^2$. Cancellation of terms on the left- and right-hand sides at the boundary is equivalent to solving the modified problem

$$\frac{\partial^2 u}{\partial z^2} = \frac{\partial \omega}{\partial z}$$

in $(0^+, H)$ with the Neumann condition $\mathrm{d}u/\mathrm{d}z = 0$ at 0^+. This yields the correct initial solution $u(z) = 0$ everywhere except at the plate surface, where $u = 1$ from.

For comparison, in the stream function vorticity ($\psi - \omega$) formulation in two dimensions, the tangential velocity is derived from the normal gradient of ψ. It is not usual at a wall to employ the tangential slip velocity (gradient of ψ) as boundary condition for $\nabla^2\psi = -\omega$ but rather $\psi = \text{constant}$. A stream function vorticity solution may be obtained with a surface gradient condition but a similar analysis to the above again shows it is required to maintain consistency between the vorticity boundary conditions and Poisson equation.

3.2.2. Calculations on Lagrangian frame. Having calculated the velocities and vorticities on the mesh points, these results are interpolated back onto the Lagrangian frame to track the particles.

3.2.2.1. The particle dynamics. The interpolation scheme used is based on the volume weighting. The vortices are assigned to the eight surrounding mesh points by projection of the vortex strengths of the particles in the cell

$$\vec{\omega}_i = \vec{k}_p \frac{V_i}{V^2} \quad i = 1, \ldots, 8 \tag{14}$$

where $V = h^3$ (for a uniform mesh, $\Delta x = \Delta y = \Delta z = h$).

The vorticity change due to diffusion and stretching on the mesh points is interpolated back onto the particles by volume weighting. Thus the new strength of a particle is given by

$$\vec{k}_p^{n+1} = \vec{k}_p^n + \sum_{i=1}^{8} \Delta\omega_i \frac{V_i}{V_{ti}} h^3 \tag{15}$$

where h is the cell size and V_{ti} is the sum of the volumes contributions, V_i from all particles which contribute to the vorticity at node i. The velocity of the particles is also obtained by the same interpolation scheme, giving

$$\vec{u}_p = \sum_{i=1}^{8} \vec{u}_i \frac{V_i}{V} \tag{16}$$

The particles positions are updated by

$$\vec{x}_p^{\,n+1} = \vec{x}_p^{\,n} + (\vec{u}_p^{\,n}) \cdot \Delta t \tag{17}$$

3.2.3. Outline of the PIC scheme. Initialization

(1) The initial vorticity is first discretized as a set of particles, $\{\vec{k}_p^0\}$

$$\vec{\omega}^0 \to \{\vec{k}_p^0\}$$

then the vorticity strengths of the particles are projected onto the mesh, using a volume based weighting interpolating

$$\{\vec{k}_p^0\} \to \vec{\omega}_{i,j,k}^0$$

(2) The velocity components on the mesh are found from

$$\nabla_{\mathrm{D}}^2 \vec{u}_{i,j,k}^0 = -\nabla_{\mathrm{D}} \wedge \vec{\omega}_{i,j,k}^0$$

where ∇_{D}^2 and ∇_{D} are a discrete approximation to ∇^2 and ∇.

Update

The following sequence advances the flow over one time step:

(3) Interpolate $\vec{u}_p^n$ from $\vec{u}_{i,j,k}^n$ and move particles

$$\vec{x}_p^{\,n+1} = \vec{x}_p^{\,n} + (\vec{u}_p^{\,n}) \cdot \Delta t$$

(4) Project particle strengths on to the mesh vorticity

$$\vec{\omega}_{i,j,k}^* = \mathrm{P}\{\vec{k}_p^n(\vec{x}_p^{\,n+1})\}$$

(5) Solve for the diffusion and stretching of vorticity on the mesh

$$\frac{\vec{\omega}_{i,j,k}^{n+1} - \vec{\omega}_{i,j,k}^*}{\Delta t} = L_{\mathrm{D}}(\vec{\omega}_{i,j,k}^n) + L_{\mathrm{S}}(\vec{\omega}_{i,j,k}^n) = \Delta\vec{\omega}^{n+1}/\Delta t$$

where L_{D} and L_{S} are the discrete diffusion and stretching operators and level * corresponds to an intermediate time level.

(6) Backproject the change in nodal voriticity ($B\{\Delta\vec{\omega}\}$) to particles

$$\{\vec{k}_p^{n+1}(\vec{x}_p^{n+1})\} = \{\vec{k}_p^n(\vec{x}_p^{n+1})\} + B\{\Delta\vec{\omega}_{i,j,k}^{n+1}\}$$

(7) Create new particles on empty nodes, if vorticity > tolerance

$$\{\vec{k}_p^{n+1}\} \leftarrow \{\vec{k}_p^n\} \cup \{\vec{k}_p^c\}$$

where $\vec{k}_p^c$ are newly created particles.

(8) Solve for the velocity field which corresponds to the new vorticity field

$$\nabla_D^2 \vec{u}_{i,j,k}^{n+1} = -\nabla_D \wedge \vec{\omega}_{i,j,k}^{n+1}$$

(9) Set vorticity boundary condition

$$\vec{\omega}_{i,j,k}^{n+1}\big|_{\text{surface}} = \nabla_D \wedge \vec{u}_{i,j,k}^{n+1}$$

4. NUMERICAL RESULTS

4.1. Validation of the method

In the numerical test case, the solutions of an incompressible viscous fluid in a square and cubic cavity where the top wall is driven by a constant velocity $U_0 = 1$ are presented. The comparison of the values of velocity extrema along the centerlines of the cavity, the vorticity at the center of the cavity, and the vorticity at location $x = 0.5$ on the moving wall, with the numerical result [31,32] for various Reynolds numbers are provided in Table I. Table II gives the properties of the primary vortex. For the cubic cavity flows, computational results for the Reynolds results 100 and 400 are reported, and compared with the results of References [21,33]. The comparisons of the position of the vortex core in the y–z plane at $x = 0.5$ is listed in Table III. It is clear that the present results are in good agreement with the benchmark results.

Table I. Comparison of some characteristic values of the cavity flow

	$Re = 100$			$Re = 1000$		
	Present	Ref. [31]	Ref. [32]	Present	Ref. [31]	Ref. [32]
$ux_{\max}$	0.213	0.2109	0.2140	0.348	0.3829	0.3886
$z_{\max}$	0.456	0.4531	0.4581	0.172	0.1719	0.1717
$uz_{\max}$	0.179	0.1753	0.1796	0.373	0.3710	0.3770
$x_{\max}$	0.762	0.7656	0.7630	0.842	0.8437	0.8422
ω (0.5, 0.5)	1.171	—	1.1744	2.059	—	2.0672
ω (0.5, 1.0)	6.567	6.5745	6.5641	14.87	14.8901	14.7534

Table II. Comparison of the center (x, y) of the primary vortex and its streamfunction ψ and vorticity ω

	$Re = 100$		$Re = 400$		$Re = 1000$	
	Present	Ref. [31]	Present	Ref. [31]	Present	Ref. [31]
ψ	−0.104	−0.1034	−0.114	−0.1139	−0.118	−0.1179
ω	3.176	3.1665	2.296	2.2947	2.053	2.0497
x	0.618	0.6172	0.555	0.5547	0.533	0.5313
y	0.735	0.7344	0.606	0.6055	0.565	0.5625

Table III. Comparison of the location of vortex core for three-dimensional lid-driven cavity flows in the y–z plane at $x = 0.5$

	$Re = 100$		$Re = 400$		
	Present	Ref. [31]	Present	Ref. [21]	Ref. [33]
x	0.5	0.5	0.51	0.5	0.5
y	0.31	0.30	0.18	0.197	0.172
z	0.36	0.36	0.23	0.227	0.220

4.2. Application of the method: normal impingement of a vortex ring on a wall

The normal impingement of a laminar vortex ring on a solid surface has studied experimentally and analytically by Walker *et al.* [34] and more recently experimentally by Chu *et al.* [35]. In a numerical simulation, Orlandi and Verzicco [36] have presented detailed computational results by solving the Navier–Stokes equations and comparing with some of the experimental observations of Walker *et al.* [34]. The characteristics of a ring depend primarily on its diameter D_0 and either the propagation velocity V_0 or circulation Γ_0; thus the ring Reynolds numbers may be defined either in terms of an initial diameter and velocity, $Re_v = V_0 D_0/\nu$ or circulation $Re_\Gamma = \Gamma_0/\nu$. The behavior of a ring also depends on the distribution of vorticity within the core. Walker *et al.* [34] assumed a circular core of Kelvin Hicks type, as does Reference [36], whilst the measurements of Chu *et al.* [35] suggested a degree of ellipticity under experimental conditions. Chu *et al.* [35] find $Re_\Gamma = 2.4 Re_v$, whilst in choosing $r_0 = 0.59$ cm, $a/r_0 = 0.413$ and $r_0 a^2 = 0.0333$ cm^3, to match the conditions of References [34,36] find $Re_\Gamma = 2.32 Re_v$.

Boundary layer response: One of the first experimental investigations that interpreted the rebound of a trailing vortex from a solid surface was that of Harvey and Perry [37]. We had studied the vortex dipole rebound from a solid surface [12] and obtained good agreement between experiments and numerical results. The results showed how the boundary layer induced by the vortex dipole separated and how this separated layer finally rolls up to form a secondary vortex dipole with opposite vorticity from that of the vortex dipole.

The explanation of Harvey and Perry [37] was extended for the normal ring–wall impingement [34]. As shown by Walker *et al.* [34], when the vortex ring approaches the wall, it induces a surface boundary layer, which undergoes separation and explosive growth, leading to the

ejection of vorticity. The ejected (secondary) vorticity is oppositely signed to that of the primary ring and rolls up into a secondary ring in analogous fashion to the dipole case. The secondary ring rolls around and over the primary ring until it is inside it and at sufficiently high Reynolds number it is later ejected from the surface. Before this final stage again at a high enough Reynolds number a tertiary ring also rolls up from the surface and interacts with the secondary ring. For $Re_v > 1000$, the secondary ring becomes unstable with azimuthal disturbances amplifying. Walker *et al.* [34] consider in detail rings with Re_v of 564 and 1250, Orlandi and Verzicco [36] simulates a ring with $Re_v = 1250$, and Chu *et al.* [35] provide experimental results for Re_v approximately 750. In all of the cases studied, the complex process of vortex induced separation develops from the narrow band of boundary layer vorticity produced by the wall no-slip condition as the vortex ring approaches a solid wall.

4.2.1. Initial discretization of a vortex ring. The details that are common to all undisturbed ring computations presented in the paper are given in Reference [13]. For the instability investigations of the disturbed vortex ring a sinusoidal perturbation in the radial direction was added. Thus, the vortex particles positions are functions of the angle α and θ, i.e.

$$\vec{x}(\alpha, \theta) = \begin{pmatrix} R_s \cos\alpha \\ R_s \sin\alpha \\ 0 \end{pmatrix} \tag{18}$$

where $R_s = R_m + \varepsilon \sin\beta$ and $R_m = R + r_c \cos\theta$.

$$\beta = k\alpha \tag{19}$$

where k is wave number and ε is the amplitude of the perturbation. The new vorticity vector is chosen normal to the cross section, thus the orientation $\vec{n}$ is given by

$$\vec{n}(\alpha, \theta) = \frac{\dfrac{\mathrm{d}\vec{x}(\alpha, \theta)}{\mathrm{d}\alpha}}{\left|\dfrac{\mathrm{d}\vec{x}(\alpha, \theta)}{\mathrm{d}\alpha}\right|} \tag{20}$$

$$\vec{n}(\alpha, \theta) = \frac{1}{q} \begin{pmatrix} -R_l \sin\alpha - \varepsilon \sin\alpha \sin\beta + \beta \cos\alpha\cos\beta \\ R_l \cos\alpha + \varepsilon \cos\alpha \sin\beta + \beta \sin\alpha \cos\beta \\ 0 \end{pmatrix} \tag{21}$$

where $q = \sqrt{R_l^2 + \beta^2 + \beta^2 R_l \varepsilon \sin\beta + \varepsilon^2(1 - k^2)\sin^2\beta}$.

In three dimensions, each vortex particle has to be assigned a volume. Thus

$$\mathrm{d}v = \int_{\alpha_1}^{\alpha_2} \int_{\theta_1}^{\theta_2} \int_{r_1}^{r_2} R_s \, \mathrm{d}\alpha(r \, \mathrm{d}\theta) \, \mathrm{d}r \tag{22}$$

$$\text{vol} = (r_2 - r_1)\left[\begin{array}{c}(\theta_2 - \theta_1)\Delta\alpha \cdot R\left(\dfrac{r_2 + r_1}{2}\right) + \Delta\alpha(\sin\theta_2 - \sin\theta_1) \\ \left(\dfrac{r_1^2 + r_1 r_2 + r_2^2}{3}\right) - \dfrac{\varepsilon(\theta_2 - \theta_1)}{n}\left(\dfrac{r_2 + r_1}{2}\right)(\cos\beta_2 - \cos\beta_1)\end{array}\right] \tag{23}$$

Finally, the intensity of vorticity of each vortex particles is given by

$$\vec{k}_p = \frac{2\pi R\Gamma}{N_{\text{tot}}} \tag{24}$$

4.2.2. Weak rings ($Re_v < 1000$). For the first computations, the ring at Re_v of 750 was considered. The ring is described by 100 sections, each of 200 particles, projected onto a $128 \times 128 \times 200$ mesh, exponentially stretched near the wall. The initial data were made to be close to the experimental results but an exact match is difficult when in the computation the ring is suddenly inserted close to the wall. The initial vorticity distribution for the simulation at $Re_v = 750$ is shown in Figure 1(a). The physical dimensions of the computational domain were $128 \times 128 \times 102$ mm in streamwise, spanwise and normal directions respectively. Figure 2 compares the visualization results of Chu *et al.* [35] with the computed vorticity contours at similar stages ending at the ejection of the secondary ring. The peak vorticity in the latest stage shown is approximately 12 in both primary and secondary vortices in reasonable agreement with the measurements [35].

For a second computation the initial condition was changed slightly to a more elliptical section and (with 'a' representing the semi-minor axis of the core rather than the radius) the ratio $a/r_0 = 0.413$. The initial vorticity distribution in shown in Figure 1(b). An exponentially stretched mesh of $128 \times 128 \times 200$ was used again with 100 sections to define the ring. The physical grid spacing for the computation was $\Delta x = \Delta y = 1.5$ mm, the center was at $(x_0, y_0, z_0) = (3D_0, 3D_0, 1.5D_0)$, and after an initial 100 time steps with $\Delta t = 0.01$ s, Δt was reduced to 0.003 s. Marker particles were placed at four sections (0, 90, 180, and 270°) in the ring core to simulate the experimental dye. By measuring the propagation velocity, this ring is found to have the slightly different Re_v of 840.

Figure 3 shows the evolution of the vorticity contours. The enlargement of the vorticity contours at times $t = 0$, 0.9, 2.1 and 3.6 s are shown in Figure 4. When the primary vortex ring

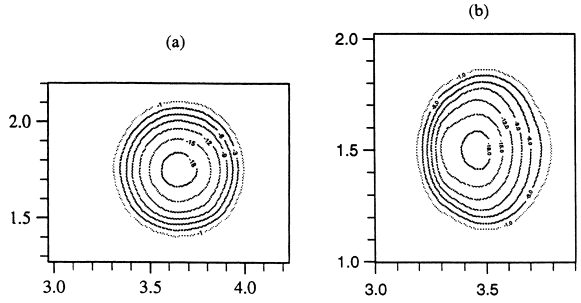

Figure 1. The initial vorticity distribution of ring at (a) $Re_v = 750$, (b) $Re_v = 840$.

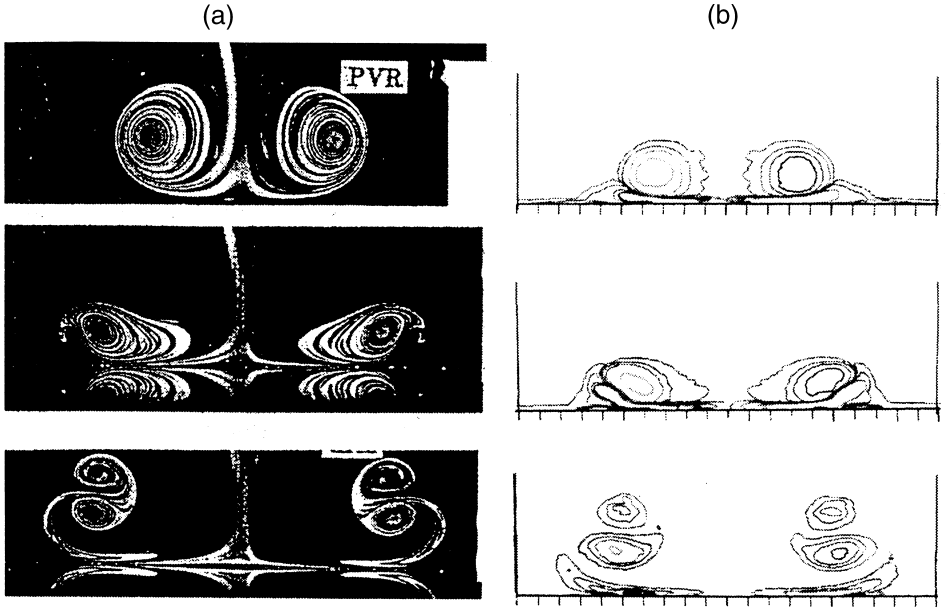

Figure 2. Viscous rebound of a vortex ring from a solid wall. Comparison between (a) visualization results of Chu *et al.* [35] (PVR: primary vortex ring), (b) the present numerical results.

approaches the wall, a thin vorticity layer is generated at the wall to counter the velocity induced by the primary vortex ring at the surface. As the primary ring gets closer to the solid wall, the induced vorticity layer strengthens. The definition of $t = 0$ for the ring–wall interaction is somewhat arbitrary and we simply reference the computed results to the first figure in Figure 3 where the ring has approximately stopped. At $t = 0.9$ s, the vorticity layer lifts up and slows the radial motion of the primary ring. With time increasing, this raised vorticity layer rolls up and forms a secondary ring. At later stages of the mutual interaction of these two rings, the secondary ring moves in a circular trajectory and eventually moves into the interior space surrounded by the primary ring. Isovorticity surfaces, for $|\omega| = 1.0$, are shown in Figure 5 for the latest time shown in Figure 3. The surfaces are coded according the orientation of the azimuthal vorticity and the primary (dark), secondary and tertiary (light) rings are shown.

In order to examine the comparison with the experimental results [34], we run the test case with the Reynolds number, $Re_v = 564$. The physical dimensions of the computational domain were (70.8, 70.8, 47.2) mm, in x-, y- and z-directions respectively. The center of the ring is $(x_0, y_0, z_0) = (35.4, 35.4, 11.8)$ mm. Marker particles were placed at two sections (0 and 180°) in the core to simulate the experimental dye.

A time sequence of the positions of the marker particles which show the vortex ring rebound from the wall at $Re_v = 564$ is given in Figure 6. Comparison of the results for marker particle

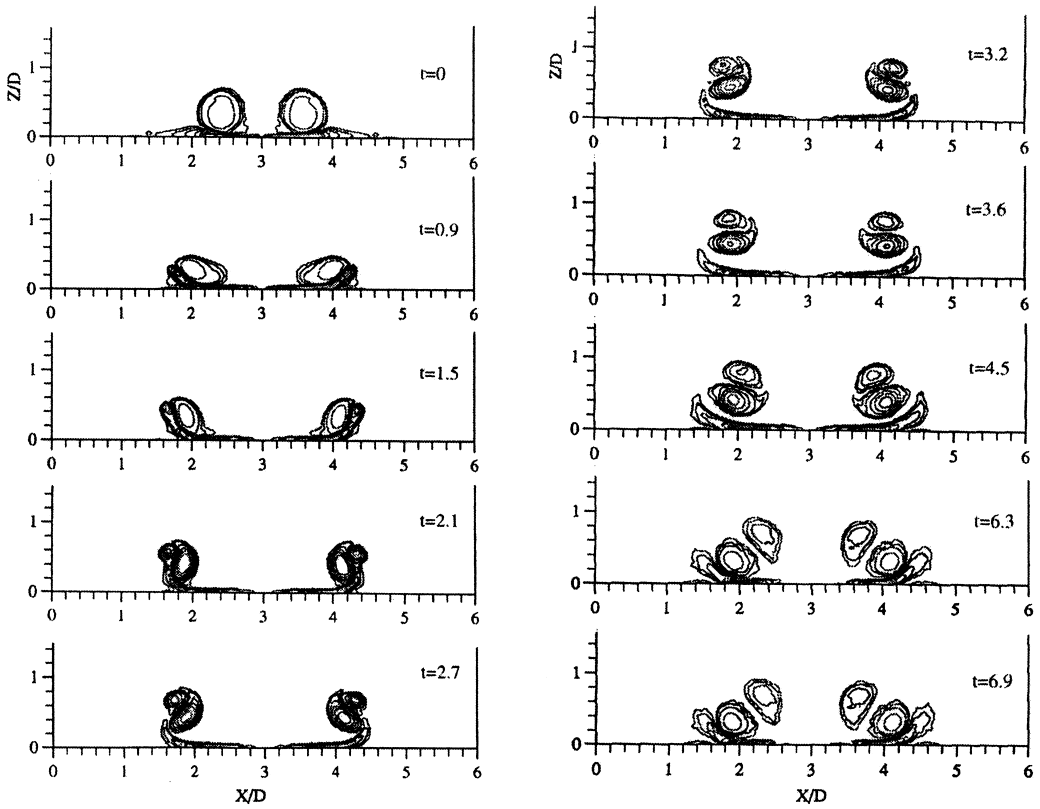

Figure 3. The evolution of vorticity contours for normal impingement of a vortex ring on a wall at $Re_v = 840$.

position with the experimental visualization results [34] shows good agreement. Figure 7 shows a comparison for the trajectory of the center of the primary ring core at $Re_v = 564$ with the experimental [34], numerical [36] and the present results. The agreement is again quite good.

As the vortex ring approaches the solid wall a vorticity layer is induced which has an opposite circulation to that of the primary ring. Cancellation of the vorticity by diffusion between the edge of the induced boundary layer and the primary ring results in the decrease of the circulation of the primary ring. With time increasing, the circulation of the primary ring gradually decreases and by $t = 0.25$ s the diameter of the vortex ring has increased significantly implying that the core has undergone considerable stretching. At this stage, the separation of the boundary layer causes the induced surface vorticity layer to lift up from the wall and form a secondary ring. At $t = 0.75$ s the radial outward motion of the primary ring is slowed eventually causing the characteristic kink in the trajectory of the core (Figure 7). In the meantime, the primary ring which is orbited by the secondary ring, rebounds a little from the

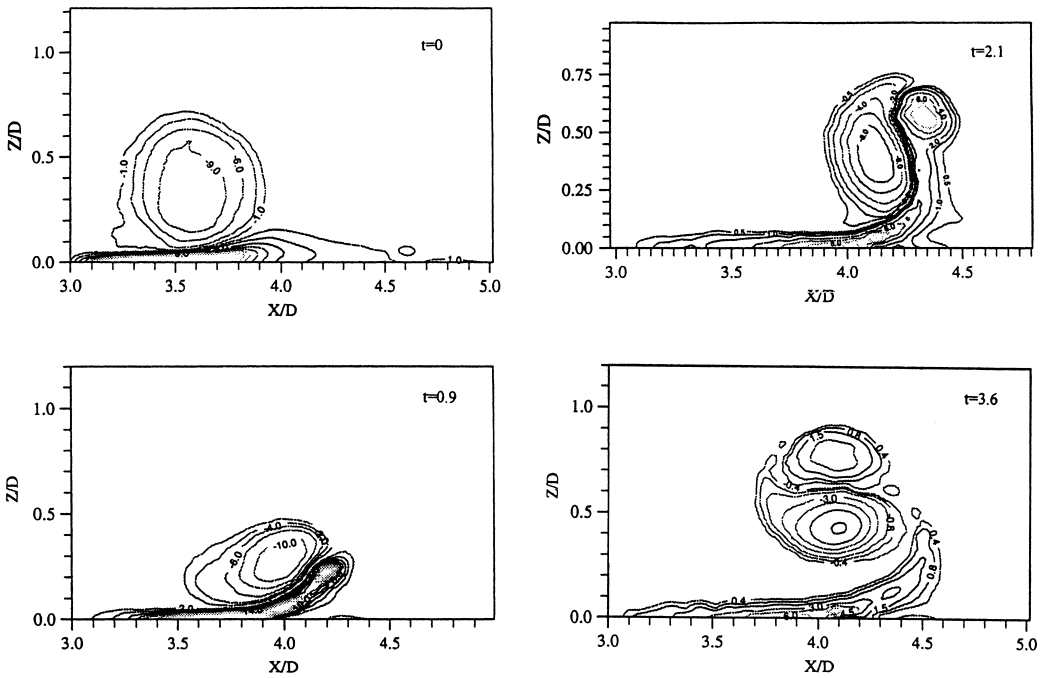

Figure 4. Contours of vorticity for normal impingement of a vortex ring on a wall at $Re_v = 840$.

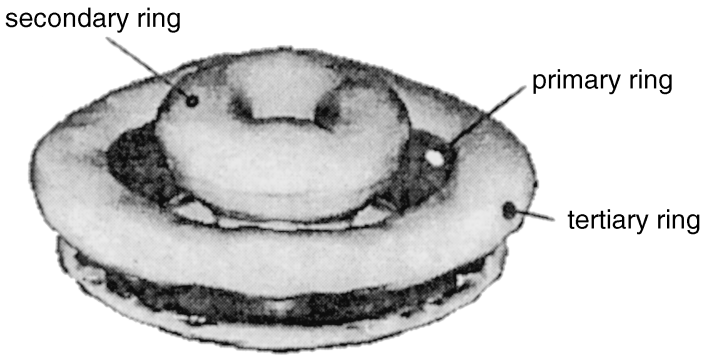

Figure 5. Isovorticity surface $|\omega| = 1.0$ for normal ring impact on a wall at $Re_v = 840$.

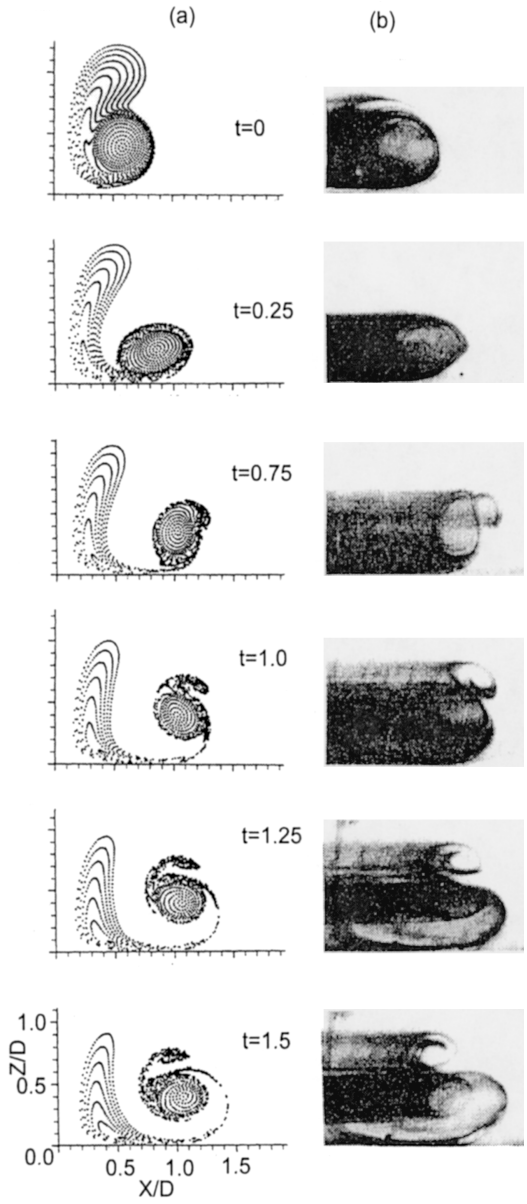

Figure 6. Vortex ring impacting a wall at $Re_v = 564$. (a) The present PIC results, computation visualized by placing marker particles at zero degree of the vortex ring and (b) the experimental results of Walker *et al.* [34].

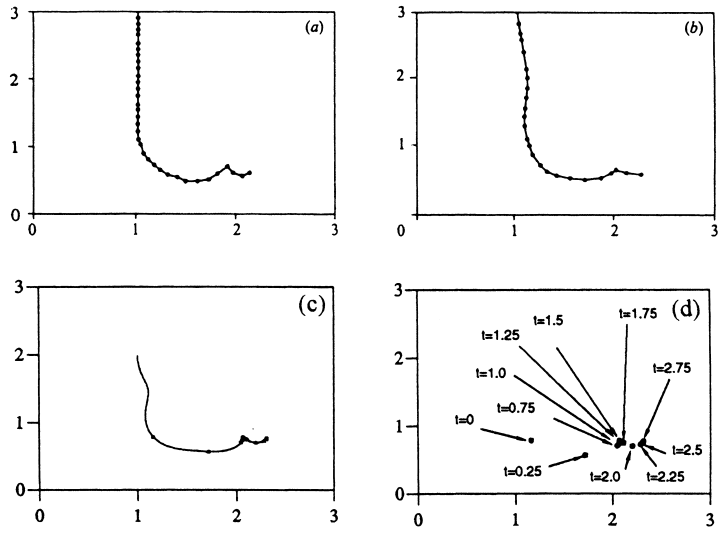

Figure 7. The trajectory of the center of the primary ring at $Re_v = 564$. (a) Experimental result of Walker *et al.* [34], (b) numerical result of Orlandi and Verzicco [36], (c) and (d) present results.

wall. The radial displacement of the primary ring is thus halted whereas for inviscid flow it would increase continually.

At the stages of $t = 1.0$, 1.25, and 1.5 s the secondary ring rolls up and over the primary ring. At $t = 1.5$ s the trajectory of the ring core reaches it highest position. In succeeding stages, the secondary ring moves towards the center of the primary ring. At $t = 1.75$ s the primary and secondary rings both approach the wall. At this stage, the position of the ring core drops down. At $t = 2$ s the primary ring is closest to the wall again and it induces a further separation and boundary layer eruption in the form of a tertiary vortex which causes a secondary rebound of the primary vortex. From Figure 7, the present numerical simulation captured this phenomenon quite clearly.

Comparison of the present results (Figure 6) with Walker's results for this stage (i.e., $t = 2$ s) show the primary vortex ring is closest to the wall for both results. At $t = 2.25$, 2.5 and 2.75 s the primary ring undergoes a second rebound from the wall (Figure 7(c), (d)).

4.2.3. Strong ring ($Re_v > 1000$). The case of $Re_v = 1250$ was also simulated using the same computational domain and conditions as $Re_v = 564$. Comparison of the numerical results (Figure 8) with the visualization results [34] again show good agreement. The experiment shows that instabilities develop and the flow is no longer axisymmetric at higher *Re*. To perform fully three-dimensional simulations and to study the development of the azimuthal instabilities for a vortex ring impacting a solid wall an initial radial disturbance has been imposed on the vortex ring with wave number $n = 5$ and amplitude $\varepsilon = 0.02r_0$.

This perturbation is similar to that used by Knio and Ghoniem [6] for the case of free rings. The ring is described by 300 sections each of 841 particles with $a_0 = 0.24$ cm whilst the ring radius was set to be 0.59 cm.

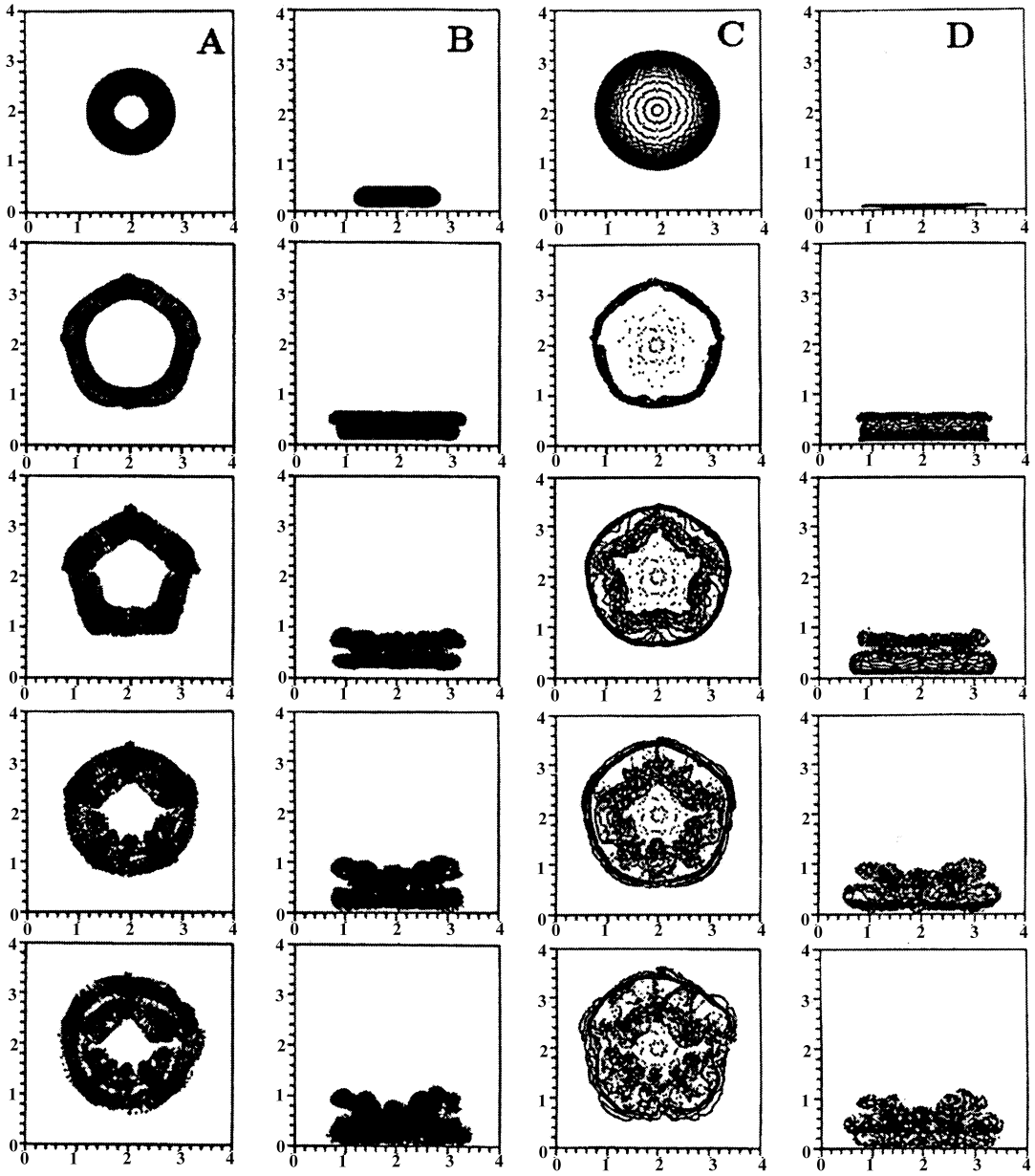

Figure 8. Vortex ring with disturbance impacting a wall at $Re_v = 1250$. (A) and (B): computation visualized by placing marker particles in vortex ring. (C) and (D): computation visualized by placing a layer of marker particles near a wall. Results are 0.166 s apart.

To visualize the vortex ring, impact marker particles are placed on the vortex ring and a layer of marker particles is also placed near the wall. The evolution of the vortex ring with a disturbance is shown in Figure 8(A) and (B) for marker particles placed in the core, whilst the results for the layer of marker particles near the surface is shown in Figure 8(C) and (D) and may be compared with the corresponding experimental results [34]. From Figure 8, wavy instabilities are observed to occur in the secondary vortex ring ($t = 0.332$ s, side view). As time increases, the amplitude of the azimuthal waves also increases and three-dimensionality becomes more pronounced. The azimuthal instabilities were observed clearly in the secondary vortex ring, as shown in Figure 8, where the detailed structure of the wave instability of the primary vortex is not so visible. To visualize more clearly the wave instabilities of the primary vortex ring, marker particles are placed on two circles of the ring with radius r_0 and $r_0 + a$ (i.e., Figure 9, dark and light circle) respectively. The light circle of marker particles rotates about the black center core circle and for $t = 0.166$ s (corresponding to the second frame in Figure 9) it is seen to lie on the surface. The expansion of the core of the primary ring is also quite clear and the frames clearly show that the disturbance to the center of the ring rotates about the ring axis. Hence, the disturbance appears to have vanished, but in the elevation view (on the right) we can see that at this instant, the disturbance is mostly in the vertical plane. In the next frame of the simulation, the disturbance has amplified and in the following one, $t = 0.664$ s, the outer circle of markers is being swept around by the nearby loops of concentrated vorticity which develop in the secondary ring. The third and fifth frames of Figure 8 also show the development of strong wavy disturbances in the secondary ring from about $t = 0.332$ s. They also show the concentrations of particles in patches in the space within the primary ring as the loops develop in the secondary ring. Walker *et al.* [34] showed in their experiments that the instability in the secondary vortex ring ultimately induces an apparent waviness in the primary ring. They also showed that the instability appears to be initiated in the secondary ring and to be associated with compression of the primary ring. The computed results (Figures 8 and 9) are in good agreement with the description of the wave instability of Walker *et al.* [34]. We also observed the occurrence of kink phenomena between the primary and secondary vortex ring. The interactions of secondary, tertiary and primary rings lead to the kink instabilities. Figure 10 shows the isovorticity surface of $|\omega| = 4$ at $t = 0.664$ s after impact, clearly showing this occurring.

5. CONCLUSIONS

In three-dimensional flow, not only are mesh solvers based on vorticity formulations less frequently applied than those using primitive variable formulations, but vortex particle methods are even less used, although they have useful potential. This paper describes a new vortex PIC method and solution algorithm along with details of the numerical implementation for the simulation of unsteady incompressible viscous wall-bounded flow and its application to the vortex ring–wall interaction problem. The procedures to treat viscous diffusion and stretching/tilting were described and it was shown how surface boundary conditions, in particular the generation of vorticity, can be incorporated in a convenient manner.

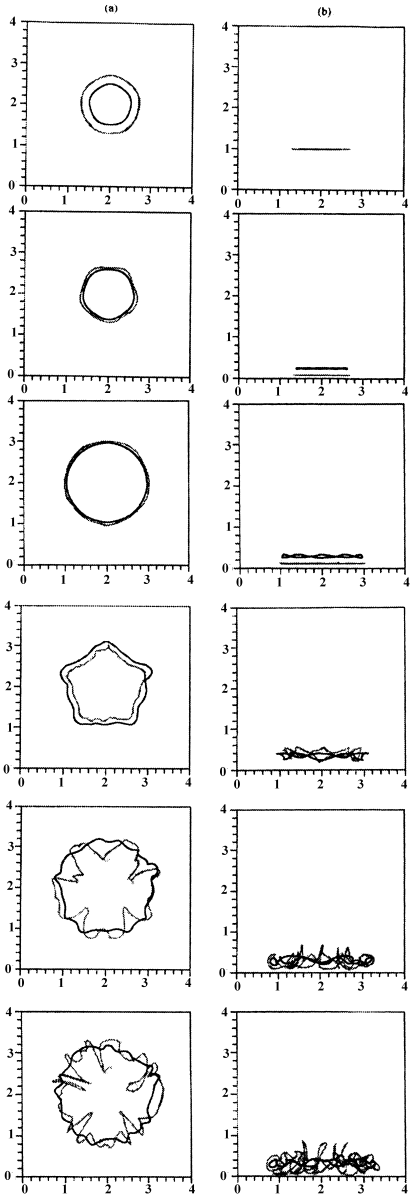

Figure 9. Vortex ring with disturbance impacting a wall at $Re_v = 1250$, computation visualized by placing marker particles in two circles of ring with radius r_0 (dark) and $r_0 + a$ (light): (a) top view, (b) side view. Results are 0.166 s apart.

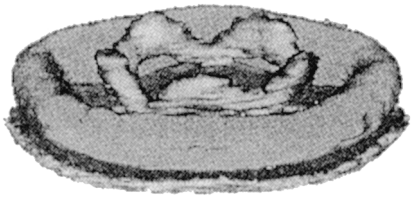

Figure 10. Isovorticity surface $|\omega| = 4.0$ for normal ring impact on a wall at $Re_v = 1250$.

The normal impingement of a vortex ring on a wall was studied for both weak rings and strong rings. With the normal ring impact on a solid wall, the present numerical results were in good agreement with those of the experimental and numerical literature. The formation of the secondary and tertiary rings was discussed, and these were clearly illustrated by plotting isosurface of vorticity for the $Re = 840$ case. The trajectories of the center of the ring core also gave good agreement with the experimental and numerical results at $Re = 564$. A fully three-dimensional case was simulated by imposing a radial perturbation on the vortex ring. It was found that the use of marker particles placed on the core and a near wall layer respectively, and in two circular filaments in the ring, were useful in studying the resulting flow. The results showed the development of the azimuthal instabilities in the secondary vortex ring, which amplified the wavy instability in the primary vortex ring. Generally speaking, the vortex PIC method performs well in predictions of the vortex–wall interaction problems for three-dimensional flow configurations.

ACKNOWLEDGMENTS

Dr. D. J. Doorly is gratefully acknowledged for his encouragement and very helpful discussions. The author would like to thank the National Science Council of the Republic of China for financially supporting this research under Grant No. NSC-85-2212-E-014-015.

REFERENCES

1. Sarpkay T. Vortex element methods for flow simulation. *Advances in Applied Mechanics* 1994; **31**: 113–247.
2. Chorin AJ. Numerical study of slightly viscous flow. *Journal of Fluid Mechanics* 1973; **57**: 785–796.
3. Beale JT, Eydeland A, Turkington B. Numerical tests of 3D vortex method using a vortex ring with swirl. *Lectures in Applied Mathematics* 1990; **28**: 1–9.
4. Canteloube B. A three dimensional point vortex method for unsteady incompressible flows. In *Computational Methods in Aeronautical Fluid Dynamics*, Stow P (ed.). Oxford University Press: Oxford, 1990; 215–248.
5. Knio O, Ghoniem AF. Numerical study of a three dimensional vortex method. *Journal of Computational Physics* 1990; **86**: 75–106.
6. Winckelmans GS, Leonard A. Contributions to vortex particle methods for the computation of three dimensional incompressible unsteady flows. *Journal of Computational Physics* 1993; **109**: 247–273.
7. Rosenhead L. The formation of vortices from a surface of discontinuity. *Proceedings of the Royal Society London A* 1931; **134**: 170–192.
8. Leonard A. Vortex methods for flow simulation. *Journal of Computational Physics* 1980; **37**: 289–335.
9. Hilka M, Doorly DJ. 3-D point vortex methods for parallel flow computation. In *Parallel Computing and Transputer Applications Part II*, Valero M, *et al.* (eds). IOS Press, 1992; 1363–1372.

10. Liu CH, Doorly DJ. Velocity–vorticity formulation with vortex particle-in-cell method for incompressible viscous flow simulation, part I: formulation and validation. *Numerical Heat Transfer*, *Part B* 1999; **35**: 251–275.
11. Liu CH, Doorly DJ. Velocity–vorticity formulation with vortex particle-in-cell method for incompressible viscous flow simulation, part II: application to vortex/wall interactions. *Numerical Heat Transfer*, *Part B* 1999; **35**: 277–294.
12. Liu CH, Doorly DJ. Vortex particle-in-cell method for three dimensional unbounded viscous flow computations. *International Journal for Numerical Methods in Fluids* 2000; **32**: 29–50.
13. Hald OH. Convergence of vortex method. In *Vortex Methods and Vortex Motion*, Gustafasson K, Sethian J (eds). SIAM: Philadelphia, 1991; 33–58.
14. Dacles J, Hafez M. Numerical methods for 3-D viscous incompressible flows using a velocity/vorticity formulation, 1990. AIAA paper 90-0237.
15. Fasel H. Investigation of the stability of the boundary layers by a finite difference model of the Navier–Stokes equations. *Journal of Fluid Mechanics* 1976; **78**: 355–383.
16. Dennis SCR, Ingham DB, Cook RN. Finite difference methods for calculating steady incompressible flows in three-dimensions. *Journal of Computational Physics* 1979; **33**: 325–329.
17. Farouk B, Fusegi T. A coupled solution of the vorticity–velocity formulation of the incompressible Navier–Stokes equations. *International Journal for Numerical Methods in Fluids* 1985; **5**: 1017–1034.
18. Napolitano M, Pascazio G. A numerical method for the vorticity–velocity Navier–Stokes equations in a two and three dimensions. *Computers and Fluids* 1991; **19**: 489–495.
19. Daube O. Resolution of the 2D Navier–Stokes equations in velocity–vorticity form by means of an influence matrix techniques. *Journal of Computational Physics* 1992; **103**: 402–414.
20. Ern A, Smooke MD. Vorticity–velocity formulation for three dimensional steady compressible flows. *Journal of Computational Physics* 1993; **105**: 58–71.
21. Guj G, Stella A. A vorticity–velocity method for the numerical solution of 3D incompressible flows. *Journal of Computational Physics* 1993; **106**: 286–298.
22. Guevremont G, Habashi WG, Kotiuga PL, Hafez MM. Finite element solution of the 3D compressible Navier–Stokes equations by a velocity–vorticity method. *Journal of Computational Physics* 1993; **107**: 176–187.
23. Couët B, Buneman O, Leonard A. Simulation of three-dimensional incompressible flows with a vortex-in-cell method. *Journal of Computational Physics* 1981; **39**: 305–328.
24. Brecht SH, Ferrante JR. Vortex-in-cell simulations of buoyant bubbles in three dimensions. *Physics of Fluids* 1989; **A1**: 1166–1191.
25. Zawadzki I, Aref H. Mixing during vortex ring collision. *Physics of Fluids* 1991; **A3**: 1405–1412.
26. Saad Y, Schultz MH. GMRES: a generalized minimal residual algorithm for solving nonsymmetric linear systems. *SIAM Journal of Scientific and Statistical Computing* 1986; **7**: 856–869.
27. Gustafsson I. A class of first order factorization methods. *BIT* 1978; **18**: 142–156.
28. Eisenstat SC. Efficient implementation of a class of preconditioned conjugate gradient methods. *SIAM Journal of Scientific and Statistical Computing* 1981; **2**: 1–4.
29. Choquin J-P, Cottet G-H. Sur l'analyse d'une classe de methods de vortex tridimensionnells. *Comptes Rendus de l'Academie de Sciences*, *Paris* 1988; **306**: 739–742.
30. Rehbach C. Numerical calculation of three-dimensional unsteady flows with vortex sheets, 1978. AIAA paper No. 78-111.
31. Ghia U, Ghia KN, Shin CT. High-resolutions for incompressible flow using the Navier–Stokes equations and a multigrid method. *Journal of Computational Physics* 1982; **48**: 378–411.
32. Botella O, Peyret R. Benchmark spectral results on the lid-driven cavity flow. *Computers and Fluids* 1998; **27**: 421–433.
33. Ku HC, Hirsh RS, Taylor T. A pseudospectral method for solution of the three-dimensional incompressible Navier–Stokes equations. *Journal of Computational Physics* 1987; **70**: 439–462.
34. Walker JDA, Smith CR, Cerra AW, Doligalski TL. The impact of a vortex ring on a wall. *Journal of Fluid Mechanics* 1987; **181**: 99–140.
35. Chu CC, Wang CT, Hsieh CS. An experimental investigation of vortex motions near surfaces. *Physics of Fluids*, *A* 1993; **5**: 662–676.
36. Orlandi P, Verzicco R. Vortex rings impinging on walls: axisymmetric and three dimensional simulations. *Journal of Fluid Mechanics* 1993; **256**: 615–646.
37. Harvey JK, Perry FJ. Flowfield produced by trailing vortices in the vicinity of the ground. *AIAA Journal* 1971; **9**: 1659–1660.

